



Contents lists available at ScienceDirect

Chemical Engineering Research and Design

journal homepage: www.elsevier.com/locate/cherdiChemE
ADVANCING
CHEMICAL
ENGINEERING
WORLDWIDE

Toward computationally effective modeling and simulation of droplet formation in microchannel junctions

Roman Filimonov^{a,*}, Zan Wu^b, Bengt Sundén^b

^a LUT University, School of Engineering Science, P.O. Box 20, Lappeenranta FIN-53851, Finland

^b Lund University, Department of Energy Sciences, P.O. Box 118, Lund SE-22100, Sweden

ARTICLE INFO

Article history:

Received 29 June 2020

Received in revised form 13 October 2020

Accepted 12 November 2020

Available online 11 December 2020

Keywords:

Liquid–liquid slug flow

Droplet-based microfluidics

CFD

Volume of fluid (VOF)

Contact angle

Computational time

ABSTRACT

Droplet-based microfluidics is a widely used technology in various chemical and biological applications. Droplet formation is an essential part of droplet-based microfluidics. This work applied and summarized a combination of techniques for speeding up computational fluid dynamics (CFD) simulations based on the Volume of Fluid method for the droplet generation process. To demonstrate the efficiency of the applied techniques, numerical modeling and simulation of droplet formation in a cross-shaped square microchannel were carried out. Water–butanol and water–toluene two-phase systems were considered under various flow rate conditions. Flow visualization experiments were conducted to validate the numerical results. In addition, a parametric analysis on the influence of viscosity, interfacial tension, and three-phase contact angle on the droplet formation was carried out to demonstrate the performance of the numerical setup. The simulated fluid flow dynamics showed good agreement with the experimental data. The CFD model was also verified by simulating the droplet formation in a T-shaped rectangular microchannel. The presented setup shows promising potential for development of chips for droplet generation by testing virtual prototypes. Due to the possibility to model the droplet formation process at an acceptable computational cost, time savings in the research and design cycles can be significant.

© 2020 The Author(s). Published by Elsevier B.V. on behalf of Institution of Chemical Engineers. This is an open access article under the CC BY license (<http://creativecommons.org/licenses/by/4.0/>).

1. Introduction

Microfluidics has become an attractive field within the scientific and industrial communities. Microfluidic devices offer a number of benefits, such as smaller sample volume consumption, improved flow control, and enhanced heat and mass transfer capabilities, compared to conventional macro-scale systems. The microfluidic technology has therefore been increasingly used in various chemical and biological applications (Nguyen et al., 2019; Kandlikar et al., 2005).

Multiphase microfluidic systems have been of particular interest owing to their potential applications, such as extrac-

tion, separation and purification, and biological screening (Geng et al., 2020). The slug flow regime is one of the most common multiphase flow patterns employed in microfluidic systems. Slug flow (also known as Taylor flow) in microchannels is referred to as a two-phase flow pattern characterized by the motion of gas bubbles or liquid droplets in an immiscible carrier liquid. Liquid slugs are connected by a thin liquid film that separates gas bubbles/liquid droplets from the wall. While a considerable amount of research works on gas–liquid slug flow has been carried out, the number of studies on liquid–liquid slug flow is still quite limited (Abdollahi et al., 2017). However, using of an immiscible liquid instead of the gas phase has recently received more attention due to its application in droplet-based microfluidics - a subclass of microfluidics based on manipulation of microdroplets. Droplet-based microfluidic systems enable the

* Corresponding author.

E-mail address: roman.filimonov@lut.fi (R. Filimonov).

<https://doi.org/10.1016/j.cherd.2020.11.010>

0263-8762/© 2020 The Author(s). Published by Elsevier B.V. on behalf of Institution of Chemical Engineers. This is an open access article under the CC BY license (<http://creativecommons.org/licenses/by/4.0/>).

compartmentalization of reactions into individual droplets, allowing precise control of reaction time, rapid mixing (within a millisecond scale), and low reagent consumption (femto-liter to microliter volumes), among other advantages. Some examples of applications of droplet-based microfluidics are protein crystallization, DNA analysis, synthesis of molecules, and electronics cooling (Song et al., 2006; Bordbar et al., 2018).

Studying slug flow experimentally is not always sufficient to obtain a comprehensive knowledge of the related flow phenomena. Furthermore, making measurements in microstructures is a difficult procedure. Computational fluid dynamics (CFD) has therefore emerged as an alternative approach to explore slug flow in microchannels. To make a direct comparison of the numerical results with the experimental ones, it is necessary that the droplet/bubble and slug lengths are the same as those in the experiments. This can be done by modeling the same bubble/droplet formation configuration (e.g., T-junctions) as that employed in the experimental setup. Such modeling requires unsteady, three-dimensional calculations which are computationally very intensive. Due to that reason, many of the numerical investigations on slug flow use predefined droplets/bubbles, omitting the formation mechanism. Numerous studies have considered axisymmetric problems in order to use two-dimensional axisymmetric domains and thus to reduce the computational demand (Gupta et al., 2009). Gupta et al. (2010), Mehdizadeh et al. (2011), and Magnini and Thome (2016) simulated heat transfer in slug flow in circular microchannels using the fixed reference frame methodology (two-dimensional axisymmetric domain). Slug flow hydrodynamics in circular microchannels was also investigated by Gupta et al. (2013), Langewisch and Buongiorno (2015), and Kumari et al. (2019), but employing the moving reference frame approach (two-dimensional axisymmetric domain). The idea of this approach is based on the fact that fully-developed slug flow is steady in a frame of reference moving with the bubble/droplet (Asadolahi et al., 2011). Thus, a single bubble/droplet surrounded by the carrier liquid is modeled only, decreasing the computation time even further. The moving reference frame has therefore been mostly adopted for studies that require three-dimensional simulations, such as those involving microchannels with non-circular cross-sections (Zhang et al., 2016; Che et al., 2015; Talimi et al., 2013; Taha and Cui, 2006). Although the aforementioned numerical approaches allow investigation of the slug flow characteristics (e.g., liquid film thickness or heat transfer), they require experiments in order to determine the bubble/droplet and liquid slug lengths to be modeled. Thus, they can only be used as supplementary methods in studies of a given slug flow.

A comparatively limited number of studies includes the bubble/droplet formation process modeling. Dang et al. (2015) carried out simulations of the bubble formation process (air-water flow) in a square microchannel with a converging shape junction. Jia and Zhang (2016) modeled the process of dissolution of CO₂ bubbles in ethanol and methanol in a cross-shaped rectangular microchannel. The droplet/bubble formation process in T-junction rectangular microchannels was investigated numerically by Qian et al. (2019), Soh et al. (2016), and Hoang et al. (2013). Wu et al. (2017a) and Lan et al. (2015) performed simulations of droplet formation in coaxial microchannels. Droplet generation was included into the CFD models by Madadelahi and Shamloo (2017) and Wang et al. (2015) to study the mixing inside

droplets flowing along serpentine microchannels. Three-phase gas-liquid-liquid (air-water-oil) slug flow in a double T-junction rectangular minichannel was simulated by Rajesh and Buwa (2018).

Despite quite extensive research efforts on exploring the droplet formation in microchannels with the aid of CFD modeling, little attention has been given to the efficiency of such simulations. As was pointed out above, numerical modeling of the droplet generation process has been associated with high computational demands. The possibility of performing simulations at reasonable time and computational expense can be regarded as one of the decisive factors for their applicability to practical tasks in the field of microfluidics. Development of a microchannel geometry that is capable of producing droplets of certain sizes is an example where numerical modeling may largely benefit the design process. Therefore, the present study aims to make a step toward enhancing the computational efficiency of CFD simulations of the droplet generation process. Specifically, this work outlines a set of measures for speeding up VOF-based simulations of the droplet formation process. To show the effectiveness of the proposed steps, droplet formation in a square microchannel of cross-shaped junction is simulated. Different liquid-liquid systems are considered and experimental data are used to validate the numerical results. The influence of flow rates, viscosity, and surface tension on the droplet formation is demonstrated. Furthermore, the numerical setup is employed to model the droplet generation in a T-shaped geometry. The simulated results are also compared with the experimental data published by Garstecki et al. (2006). The effect of the wall contact angle at the channel junction, where both liquids are in contact with the solid, is also examined.

2. Experimental setup

The experimental setup employed in the present study is similar to that used by Wu et al. (2017b) and shown in Fig. 1a.

Droplet formation was performed using a glass microchip with a cross-shaped square microchannel of hydraulic diameter $D_h = 400\ \mu\text{m}$ (Little Things Factory GmbH). The microchannel was made in borosilicate glass and sealed by a thermal bonding method. The length of the inlet channels is 15 mm, while the main channel is 105 mm long (see Fig. 1b). Deionized water was used as the continuous phase and the dispersed phase was either 1-butanol (Acros Organics, $\geq 99.99\%$) or toluene (Acros Organics, $\geq 99.95\%$). The continuous and dispersed phases were fed to the side and central inlet channels, respectively, using two high-precision syringe pumps (New Era, NE-4000). The experiments were conducted at $20 \pm 0.5^\circ\text{C}$. The densities and dynamic viscosities of water, butanol, and toluene are, respectively, $998.2\ \text{kg/m}^3$ and $0.001\ \text{kg/m}\cdot\text{s}$, $810\ \text{kg/m}^3$ and $0.00294\ \text{kg/m}\cdot\text{s}$, and $870\ \text{kg/m}^3$ and $0.00059\ \text{kg/m}\cdot\text{s}$. The interfacial tensions for water/butanol and water/toluene are 0.0018 and $0.036\ \text{N/m}$. The flow conditions are listed in Table 1. The flow rate ratios were selected based on the data from Wu et al. (2017b) to operate in the slug flow regime. The liquid-liquid flow near the junction was captured by a camera (Olympus OM-D E-M1) mounted on a microscope (Motic, SMZ-171). The videos were recorded at a resolution of 1280×720 pixels at a rate of 30 frames per second with a shutter speed of $1/8000\ \text{s}$. A fiber optic light source was utilized to illuminate the chip (Motic, MLC-150C).

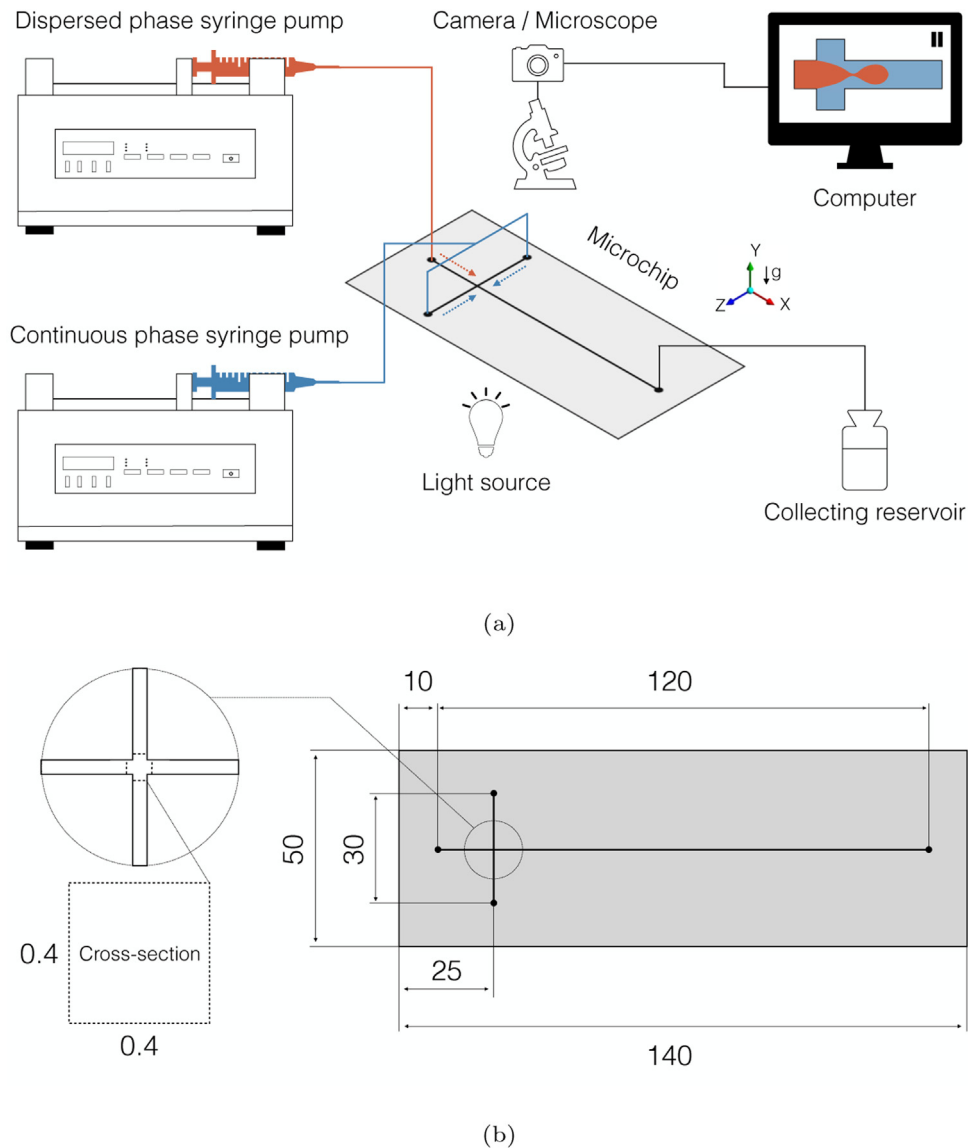


Fig. 1 – (a) Schematic diagram of the experimental setup; (b) the microchannel geometry (dimensions are mm).

Table 1 – Flow conditions. Capillary number of the continuous phase and Weber number of the dispersed phase are defined in Section 4.1.

Continuous/dispersed phase	Flow rates (ml/h)	Capillary number (continuous phase)	Weber number (dispersed phase)
Water/butanol	6.5/4	$6.3\text{e}-3$	$8.7\text{e}-3$
	8/4	$7.7\text{e}-3$	$8.7\text{e}-3$
	10/5	$9.6\text{e}-3$	$1.3\text{e}-2$
Water/toluene	4/1	$1.9\text{e}-4$	$2.9\text{e}-5$
	8/2	$3.8\text{e}-4$	$1.2\text{e}-4$

3. Numerical analysis

3.1. Computational domain and boundary conditions

In the numerical model, the original channel size was decreased in order to reduce the computational time (see Fig. S1). The lengths of the inlet and main channels were set as 0.8 and 6 mm, respectively. Due to the symmetric shape of the channel and flow pattern, the computational domain was halved by a vertical symmetry plane. The size of the domain

was further halved by a horizontal symmetry plane because the effect of gravity is negligible for small values of the Bond number ($Bo < 1$) (Jia and Zhang, 2016).

Fully developed velocity profiles were imposed at the inlets to minimize the length of the inlet channels. These profiles were determined by running steady-state single phase simulations. A zero static pressure was set at the outlet. No-slip boundary conditions were applied at the walls of the channel. At the symmetry planes, symmetry boundary conditions were applied. At the start of the simulations, the whole computa-

tional domain was filled with the continuous phase, except the central inlet channel which was completely filled with the dispersed phase.

3.2. Governing equations

To simulate the liquid–liquid slug flow, the volume of fluid (VOF) model was employed (Hirt and Nichols, 1981). This model was developed to track the position of the interface between two or more immiscible fluids. It is one of the most widely used models in the literature, and it has been shown as a robust and computationally effective approach for interface tracking (Gupta et al., 2010; Soh et al., 2016; Jia and Zhang, 2016; Zhang et al., 2016). In the VOF method, a single set of mass and momentum conservation equations is solved. The interface tracking is accomplished by solving an additional advection equation for the volume fraction. Thus, the equations for the incompressible two-phase flow can be written as follows:

$$\text{Continuity: } \nabla \cdot \vec{u} = 0 \quad (1)$$

$$\begin{aligned} \text{Momentum: } \rho \left(\frac{\partial \vec{u}}{\partial t} + \vec{u} \cdot \nabla \vec{u} \right) = & -\nabla p \\ & + \nabla \cdot \left[\mu \left(\nabla \vec{u} + \nabla \vec{u}^T \right) \right] + \vec{F}_{SV} \end{aligned} \quad (2)$$

$$\text{Volume fraction: } \frac{\partial \alpha}{\partial t} + \vec{u} \cdot \nabla \alpha = 0 \quad (3)$$

where \vec{u} is the velocity vector, p is the pressure, ρ and μ are, respectively, the volume-fraction-averaged density and viscosity of the phases, α is the volume fraction of the dispersed phase, \vec{F}_{SV} is the interfacial tension force, and ρ_c and ρ_d are the densities of the continuous and dispersed phases. The interfacial tension force, acting only at the interface, was determined according to the continuum surface force (CSF) model (Brackbill et al., 1992):

$$\vec{F}_{SV} = \frac{\rho}{\frac{1}{2}(\rho_c + \rho_d)} \sigma \kappa \nabla \alpha \quad (4)$$

where σ is the interfacial tension coefficient, and $\kappa = \nabla \cdot \hat{n}$ is the interface curvature, where $\hat{n} = \nabla \alpha / |\nabla \alpha|$ is the surface unit normal vector.

A liquid–liquid–wall interaction exists at the junction of the channel. It is therefore necessary to specify a wall adhesion angle (contact angle) (Gupta et al., 2009). The contact angle is used to calculate the interface curvature near the wall by adjusting the interface normal in the cells adjacent to the wall as follows (Brackbill et al., 1992):

$$\hat{n} = \hat{n}_w \cos \theta_w + \hat{t}_w \sin \theta_w \quad (5)$$

where θ_w denotes the contact angle, and \hat{n}_w and \hat{t}_w the unit vectors normal and tangential to the wall, respectively.

3.3. Solution methods

The equations are solved in the ANSYS Fluent 17.0 CFD software. The gradients of scalars are evaluated using the Green-Gauss node-based method. The PRESTO! interpolation

scheme is employed to compute the face pressure. The convective and diffusion terms are discretized using second-order upwind and central difference schemes, respectively. The temporal discretization of the momentum equation is done by a first order non-iterative fractional step method (Gupta et al., 2009). The non-iterative time advancement (NITA) scheme often provides a substantial speed-up to unsteady simulations compared to the iterative algorithm (Fletcher et al., 2017). The geometric reconstruction scheme based on the piecewise linear interface calculation approach of Youngs (1982) is used to represent the interface between the liquids. The sub time step size for the volume fraction equation is controlled automatically by keeping the maximum allowable Courant number (Co_{VOF}) near the interface at 0.25. The sub time step is then calculated as

$$\Delta t_{VOF} = Co_{VOF} \min \left(\frac{V}{\sum_{\text{cell}} U_f} \right) \quad (6)$$

where V is the cell volume (cell size is discussed in Section 4.1), and U_f represents the outgoing fluxes.

4. Results and discussion

4.1. Mesh and time step independence studies

ANSYS ICEM 17.0 is utilized to generate a grid for the computational domain. The calculation of interfacial tension forces is known to be more accurate on hexahedral grids comprised of elements having aspect ratio values as close as possible to 1 (cubic shape) (Gupta et al., 2009). Therefore, the domain is meshed with cubic elements. Only in the inlet channels, the element size is gradually increased in the axial direction (maximum aspect ratio of around 3) toward the inlets in order to decrease the number of cells. To determine the appropriate cell size for the simulations, grids of different densities are tested. Element sizes of $D_h/25$, $D_h/50$, $D_h/75$ and $D_h/100$ are considered for the mesh independence analysis. The analysis is performed for water at a flow rate, Q_c , of 10 ml/h (5 ml/h to each side inlet as shown in Fig. 1a) and butanol at a flow rate, Q_d , of 5 ml/h. These flow conditions correspond to the Capillary number of the continuous phase, Ca_c , of 0.0096 and the Weber number of the dispersed phase, We_d , of 0.013 (see Table 1). Ca_c and We_d are calculated as

$$Ca_c = \frac{\mu_c j_c}{\sigma} \quad (7)$$

$$We_d = \frac{\rho_d j_d^2 D_h}{\sigma} \quad (8)$$

where μ_c is the viscosity of the continuous phase, ρ_d is the density of the dispersed phase, and j_c and j_d are the superficial velocities of the continuous and dispersed phases, respectively.

Simulation results for the four mesh refinements are presented in Fig. 2a. Droplet velocity, droplet size, water slug length and droplet volume are decreased with the increase of the grid resolution. Moving from an element size of $D_h/25$ to $D_h/100$ resulted in differences of 1.33%, 2.03%, 3.01% and 2.5% between the values, respectively, for droplet velocity, droplet length, water slug length, and droplet volume. Comparing the meshes with element sizes of $D_h/50$ and $D_h/100$, the corresponding differences were 0.68%, 0.37%, 0.68% and 0.77%. As illustrated in Fig. 2b, the droplet shape remained nearly iden-

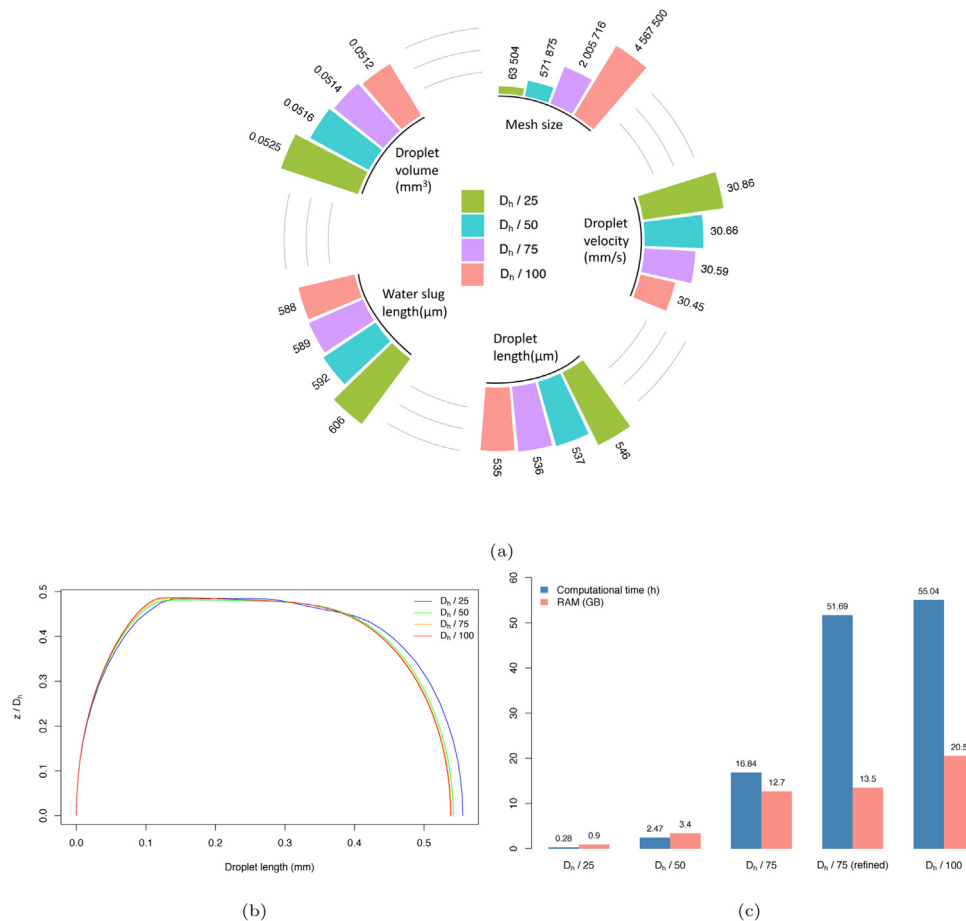


Fig. 2 – Effect of different mesh refinements at $Q_c = 10$ ml/h and $Q_d = 5$ ml/h on (a) droplet velocity, droplet length, water slug length, and droplet volume; (b) droplet interface shape; (c) computational time (wall clock time) of 3 droplets and memory usage. Droplet length is the distance between the nose and the tail of the droplet. Water slug length is the distance between two successive droplets. Both quantities are measured along the channel centerline. Interface is defined as a contour line at $\alpha = 0.5$. The simulations were run on a cluster using 10 cores of Intel Xeon E5-2690 v3.

tical for the $D_h/50$, $D_h/75$ and $D_h/100$ grids, while it deviated noticeably for the coarsest one ($D_h/25$).

It should be noted, though, that none of the tested meshes was able to provide a completely grid-independent solution. Because of a thin liquid film between the droplet and the channel boundary, a very fine near-wall grid is necessary to resolve the film region properly. According to Gupta et al. (2009), at least five elements are required across the liquid film in order to capture it. These authors also reported that if the grid resolution is too coarse, the droplet shape and liquid film can be captured by using a wall adhesion angle. As even the finest mesh ($D_h/100$) was not capable of capturing the liquid film in the present simulations, a contact angle was specified also at the walls of the main channel. While the contact angle has no effect on the droplet shape in simulations that do capture the liquid film, it affects the droplet shape in those that do not. In the present setup, a contact angle of 0° (total wetting by water) was found to have no influence on the droplet shape. It was verified by performing simulations using a sufficiently fine mesh; the near wall region of the $D_h/75$ grid was densified with ten cell layers, $1\ \mu\text{m}$ thick each. The refined grid provided a more accurate representation of the near-wall region. An undulation appeared at the rear of the droplet, which is also observed in experiments (Bretherton, 1961; Wu et al., 2017b;

Gupta et al., 2013). However, the overall effect on the slug shape was negligible (see Fig. S2).

Refining the mesh increased the number of cells and hence the computational demand. Furthermore, the time step decreased with the element size. Thus, as illustrated in Fig. 2c, both the computational time and memory usage grew sharply with decreasing the cell size. Therefore, based on both accuracy and computational demand, the $D_h/50$ grid was used in the present work. Once the droplet shape and water slug length are determined, such characteristics as mixing and heat transfer rate can be studied on finer grids employing one of the approaches proposed by Asadolahi et al. (2011).

In the grid independence analysis, the same time step size (i.e., the same maximum allowable Co_{VOF} of 0.25) as for the volume fraction equation was used for the rest of the equations. To evaluate the temporal accuracy, simulations using global Courant numbers (Co) of 0.5 and 0.75 were also carried out. A close agreement was found over the range of Co tested; the droplet and water slug lengths increased by only 3–6 μm . However, some distortions at the interface appeared at $Co = 0.75$. The computational time was reduced by roughly the same factor as the increase in the global Courant number, by 1.9 and 2.6 for Co of 0.5 and 0.75, respectively. To minimize the CPU time while preserving the accuracy, a maximum

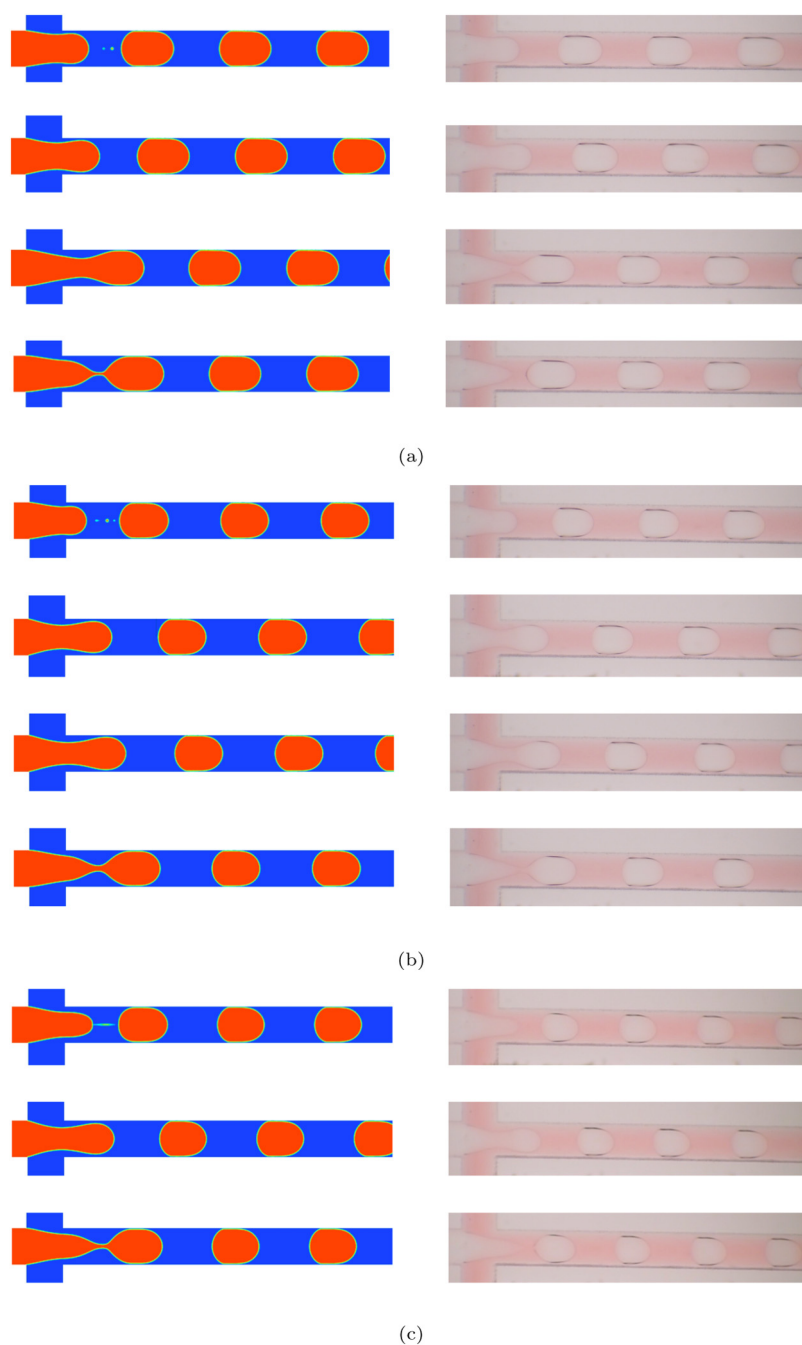


Fig. 3 – Droplet formation process obtained from simulations (left) and experiments (right) at flow rates of water and butanol, respectively, of: (a) 6.5 and 4 ml/h; (b) 8 and 4 ml/h; (c) 10 and 5 ml/h. In the experiments, minor amount of phenol red (20 drops/50 ml) was added to the continuous phase to obtain more clear images.

allowable global Courant of 0.5 was thus applied in the further computations.

4.2. Validation (water–butanol flow)

Visualization experiments were used to validate the numerical results. All the simulations were run until at least three droplets were generated in order to have a stable flow, thereby making a direct comparison with the experiments possible. In this section, water–butanol flow is considered.

Fig. 3 shows a comparison of the numerical and experimental results. Overall, the fluid flow dynamics predicted by the simulations agree well with those observed in the experiments. As can be inferred from Table 2, the trends for droplet and water slug lengths determined from the simu-

lations are consistent with the experimental ones and those determined by Wu et al. (2017b). Specifically, at a fixed flow rate ratio of butanol to water (Q_d/Q_c), the droplet length decreases with increasing flow rate of butanol (Q_d). At a fixed Q_d , the droplet length increases with Q_d/Q_c . In addition to the considered cases, water–butanol flow was simulated at flow rates of $Q_c = 4$ ml/h, $Q_d = 2$ ml/h and $Q_c = 9$ ml/h, $Q_d = 5$ ml/h in order to verify the trends. The main factor of the observed trends is that the higher flow rate of the continuous phase promotes the dispersed phase elongation and more rapid neck thinning, thus inducing the formation of shorter droplets.

The simulations overestimate both the droplet length and the water slug length. However, the difference between the results diminishes with the decrease of the flow rates. A reason for the discrepancy might be due to the fact, as described

Table 2 – Droplet and water slug lengths obtained from simulations/experiments for water–butanol flow. Droplet length is the distance between the nose and the tail of the droplet. Water slug length is the distance between two successive droplets. Both quantities are measured along the channel centerline.

Continuous/dispersed phase	Flow rates Q_c/Q_d (ml/h)	Ca_c	We_d	Simulation/experiment (difference)	
				Droplet length (μm)	Water slug length (μm)
Water/butanol	6.5/4	6.3e–3	8.7e–3	567/541 (4.7%)	500/461 (8.1%)
	8/4	7.7e–3	8.7e–3	521/459 (12.6%)	569/484 (16.1%)
	10/5	9.6e–3	1.3e–2	510/443 (14.1%)	546/450 (17.1%)

in Section 3.2, that the interfacial tension force calculation at the junction of the channel (liquid–liquid–wall interaction location) is dependent on the wall contact angle. The contact angle can thus affect the droplet formation dynamics. Therefore, to predict the droplet formation process more accurately, a correct contact angle value, which is measured experimentally, needs to be known. The effect of contact angle hysteresis may also be considered in order to obtain a more realistic droplet formation process (Fang et al., 2008). However, measuring equilibrium, advancing and receding contact angles is not a trivial procedure. Furthermore, those quantities depend on microchannel geometry, surface roughness, and local fluid conditions (Brackbill et al., 1992; Huhtamäki et al., 2018).

Thus, variations in the dispersed phase elongation are observed when applying different contact angles at the channel junction, as illustrated in Fig. 4a. As further shown in Fig. 4b, at $Q_c = 10$ ml/h and $Q_d = 5$ ml/h, the droplet length varies between 486 and 543 μm , the water slug length between 491 and 603 μm , depending on the contact angle. The lengths of droplet and water slug decrease with increasing contact angle, although at some contact angles (in the range 30–60°), the lengths deviate from the trend line, growing noticeably. Contact angles greater than 140° were not considered due to the relatively large wetting of the side channel walls by the dispersed phase thread already at 120°, which was not observed in the experiments. A similar effect of the contact angle was found at the lower flow rates. Thus, since in situ values of the contact angle were not available for the present cases, a contact angle of 70° was selected at the channel junction for the cases from Table 2.

4.3. Validation (water–toluene flow)

In the next simulations, 1-butanol was replaced by toluene. Fig. 5 compares the modeled droplet formation process with the experimental one. The simulations capture the experimentally observed formation dynamics sufficiently accurately. However, the elongation of the dispersed phase thread lasts longer in the simulations. Consequently, the predicted droplet and water slug lengths are bigger than those determined from the experiments, see Table 3. As in the water–butanol system, in situ values of the contact angle were not known; it was, however, set to 0° in the water–toluene simulations. The magnitude of the difference between the simulated and experimental lengths is therefore higher in the latter case. By setting the contact angle to 70°, for example, at $Q_c = 4$ ml/h and $Q_d = 1$ ml/h, the modeled droplet and water slug lengths are, respectively, 1243 and 5356 μm . The percentage differences between the numerical and experimental values are thus reduced to 6.6% and 12.6%, respectively. It is worth to note here that the variation of the contact angle has not been used to control the size of the droplets and water slugs but

to demonstrate its role as a parameter causing uncertainty of the simulated data. Assuming that the modeling is carried out prior to the experiment (i.e., experimental data are not available), testing of different contact angle values at the channel junction can be performed to assess possible deviations.

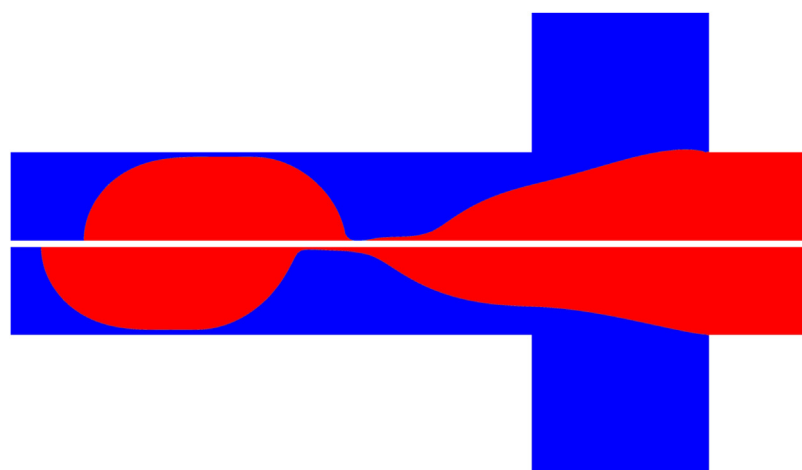
Comparing the water–butanol and water–toluene systems, markedly shorter droplets and slugs are generated in the former one. Interfacial tension is a key factor causing the difference. Specifically, the interfacial tension between water and toluene is 20 times higher than that between water and butanol, see Section 2. The interfacial tension force resists the elongation of the dispersed phase thread. Droplet formation for the water–toluene pair thus takes more time and gives more elongated droplets. The effect of viscosity and interfacial tension is investigated in the subsequent sections.

It should also be noted that the computational time for the water–toluene flow was substantially longer. At $Q_c = 8$ ml/h and $Q_d = 2$ ml/h (Table 3), the time step fluctuated around 2.5e–6 s, while for the water–butanol system at $Q_c = 10$ ml/h and $Q_d = 5$ ml/h (Table 2), the time step varied around 4e–5 s. The most likely cause of the difference lies in the higher maximum velocity at the water–toluene interface during the dispersed phase elongation (see Fig. S3). The time step was thus significantly reduced to satisfy the applied Courant number limitations. In addition, as it took more time to generate one droplet in the water–toluene system (~230 ms vs ~30 ms), it was necessary to simulate a longer time period to form the necessary number of droplets.

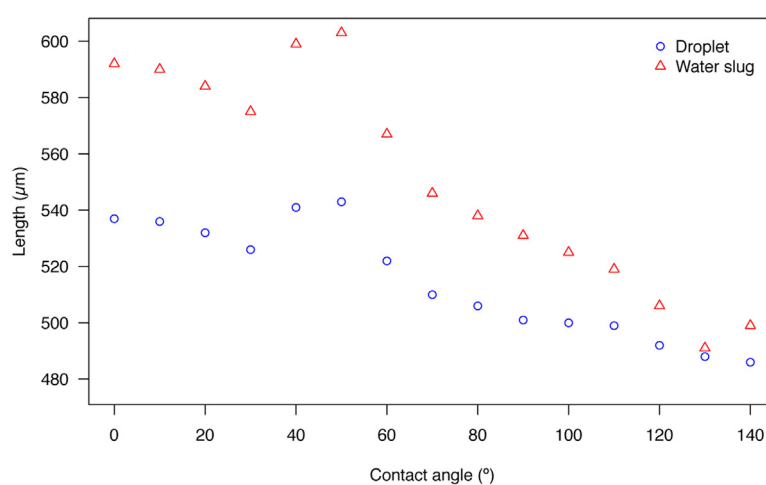
4.4. Validation (droplet formation in a T-shaped junction)

The numerical setup was additionally validated by modeling the droplet formation in a T-junction to explore the applicability of the setup to a wider range of liquid–liquid slug flows. The channel geometry was adopted from the experimental work of Garstecki et al. (2006). The main and side channels were 100 and 50 μm wide, respectively, and the channel depth was 33 μm . In the computational domain, the lengths of the inlet segment of the main channel and the side channel were set to 150 μm , while 600 μm was left for the main channel length. A horizontal symmetry plane was also defined. As in the experiments, the continuous and dispersed liquids were silicon oil and water, respectively. The densities and viscosities of oil and water are, respectively, 862 kg/m³ and 0.01 kg/m·s, and 1000 kg/m³ and 0.0009 kg/m·s. The interfacial tension between the liquids is 0.0365 N/m (Garstecki et al., 2006).

A cell size of $D_h/50$ (about 1 μm) was initially utilized to create a mesh for the domain. However, simulations at low flow rates of $Q_c = 0.028$ $\mu\text{l/s}$, $Q_d = 0.004$ $\mu\text{l/s}$ showed that the resulting grid required a very small time step to maintain Co within the limit. The computational time was thus consider-



(a)



(b)

Fig. 4 – Effect of the contact angle set at the channel junction for water–butanol system at $Q_c = 10$ ml/h and $Q_d = 5$ ml/h. (a) Dispersed phase thread just before droplet detachment at contact angles of 0° (upper half) and 70° (lower half); (b) Droplet and water slug lengths for different contact angles.

Table 3 – Droplet and water slug lengths obtained from simulations/experiments for water–toluene flow. Droplet length is the distance between the nose and the tail of the droplet. Water slug length is the distance between two successive droplets. Both quantities are measured along the channel centerline.

Continuous/ dispersed phase	Flow rates Q_c/Q_d (ml/h)	Ca_c	We_d	Simulation/experiment (difference)	
				Droplet length (μm)	Water slug length (μm)
Water/toluene	4/1	$1.9e-4$	$2.9e-5$	1367/1163 (16.1%)	5986/4720 (23.6%)
	8/2	$3.8e-4$	$1.2e-4$	1042/875 (17.7%)	4389/3120 (33.8%)

ably increased due to the large amount of steps required to advance the solution. Based on the mesh independence analysis for the water–butanol flow, the element size was therefore increased up to $\sim 1.5 \mu\text{m}$ to accelerate the calculation process at the penalty of a slight decrease of the accuracy. Consequently, the grid size was reduced from 1.3 to 0.4 million cells.

Table 4 compares the numerical results with the experimental data provided by Garstecki et al. (2006). Overall, the simulated data are qualitatively consistent with the experimental ones. The droplet and oil slug lengths are in a very close agreement in several cases. However, the droplet generation process is not captured properly for all the modeled

flow rates. For cases III and IV, the main channel was most likely not long enough for droplets to form. To provide a sufficient space, the main channel was therefore extended by $600 \mu\text{m}$. Nevertheless, only the first droplet since the start of the simulation is formed at $Q_c = 0.028 \mu\text{l/s}$, $Q_d = 0.111 \mu\text{l/s}$ (III), and generation of the following droplet is not observed. Further, for $Q_c = 0.019 \mu\text{l/s}$, $Q_d = 0.14 \mu\text{l/s}$ (IV), droplets are not formed in the simulations. Similarly to the previous case, the appearing droplet continues to fill the main channel without detaching from the dispersed phase thread (see Fig. S4). In case VI, although the numerical simulations are capable of predicting the droplet length with reasonable accuracy, the oil slug length is overestimated significantly.

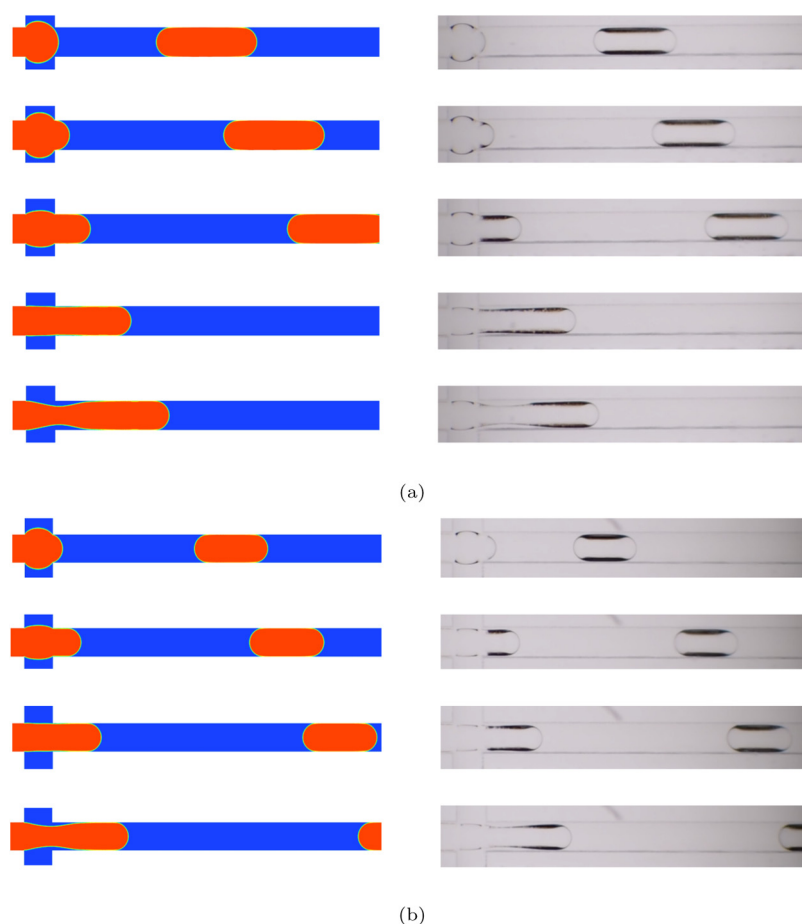


Fig. 5 – Droplet formation process obtained from simulations (left) and experiments (right) at flow rates of water and toluene, respectively, of: (a) 4 and 1 ml/h; (b) 8 and 2 ml/h.

Table 4 – Droplet and water slug lengths obtained from simulations and experiments (Garstecki et al., 2006). For $Q_c = 0.028 \mu\text{l/s}$ and $Q_d = 0.111 \mu\text{l/s}$, the experimental distance between droplets is not available. For $Q_c = 0.019 \mu\text{l/s}$ and $Q_d = 0.14 \mu\text{l/s}$, droplet formation is not observed in the simulations.

Continuous/ dispersed phase	Case	Flow rates Q_c/Q_d ($\mu\text{l/s}$)	Ca_c	We_d	Simulation/experiment (difference)	
					Droplet length (μm)	Oil slug length (μm)
Silicon oil/water	I	0.028/0.004	$2.3\text{e}-3$	$2.0\text{e}-6$	140/150 (6.9%)	766/846 (9.9%)
	II	0.028/0.05	$2.3\text{e}-3$	$3.1\text{e}-4$	291/324 (10.7%)	121/137 (12.4%)
	III	0.028/0.111	$2.3\text{e}-3$	$1.5\text{e}-3$	783/1053 (29.4%)	–/–
	IV	0.019/0.14	$1.6\text{e}-3$	$2.4\text{e}-3$	–/767	–/93
	V	0.139/0.14	$1.1\text{e}-2$	$2.4\text{e}-3$	178/176 (1.1%)	123/120 (2.4%)
	VI	0.417/0.14	$3.4\text{e}-2$	$2.4\text{e}-3$	87/110 (23.3%)	157/403 (87.8%)

It is worth to note that by increasing the contact angle at the channel junction to, for example, 40° prevents the droplet formation in case III. The limitations of the numerical model may thus be linked to the use of a constant contact angle, 0° in the considered cases. The effect of contact angle hysteresis can therefore be critical for the accurate prediction of droplet formation over a wide range of flow conditions. Advancing and receding contact angles are also typically defined experimentally. Performing in situ measurements of the contact angles is usually difficult or even impossible. The advancing and receding angles are influenced by the fluid properties, local flow conditions, inertial and interfacial forces, and channel surface properties. Therefore, the values obtained from the ex situ conditions may not correspond to the actual ones (Fang et al., 2008; Yokoi et al., 2009). Introducing a dynamic contact angle model into the numerical setup

can thus be identified as a subject for more thorough investigation.

Wall clock times for the modeling of three droplets were approximately 80, 18, 3.5 and 2 h for cases I, II, V and VI, respectively. The formation of a single droplet (case IV) took about 14 h. These simulations were performed on a cluster using 10 cores of Intel Xeon Gold 6230.

4.5. Effect of viscosity

The validity of the numerical setup is investigated further by varying the properties of the working liquids. This section presents the effect of the viscosities of the dispersed and continuous phases. First, for the cases in Table 2, the viscosity of butanol was only altered while the other properties were kept unchanged. The simulations show that both the droplet length

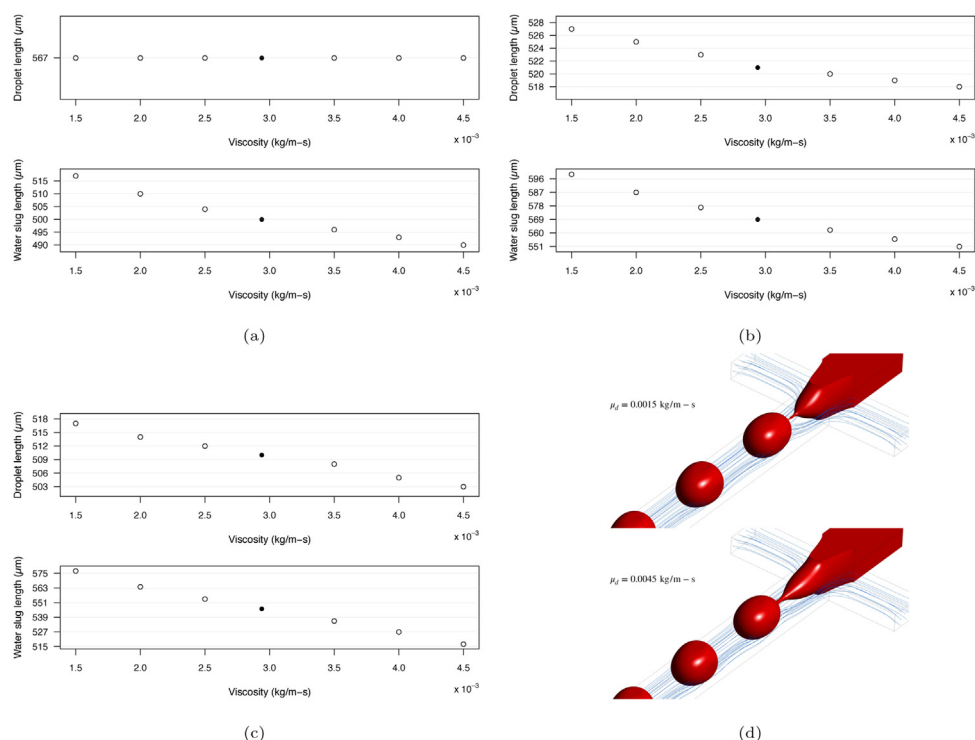


Fig. 6 – Effect of the dispersed phase viscosity on the droplet and water slug lengths for water–butanol flow. (a) $Q_c = 6.5$ ml/h, $Q_d = 4$ ml/h; (b) $Q_c = 8$ ml/h, $Q_d = 4$ ml/h; (c) $Q_c = 10$ ml/h, $Q_d = 5$ ml/h; (d) less viscous (top) and more viscous (bottom) dispersed phase at $Q_c = 10$ ml/h, $Q_d = 5$ ml/h. Filled circle denotes the original viscosity of butanol.

and the water slug length decrease with the increase of the viscosity of the dispersed phase, see Fig. 6a–c. As illustrated in Fig. 6d, increasing the dispersed phase viscosity results in a lower resistance to the elongation in the main channel. The more viscous dispersed phase thread thus penetrates farther into the continuous flow. Consequently, the droplet formation time is shortened (i.e., the distance between successive droplets is shortened) and, therefore, the droplet size becomes smaller, which is in agreement with the experimental findings of Wu et al. (2017b).

Effect of the dispersed phase viscosity is, however, most pronounced at higher flow rates. At $Q_c = 10$ ml/h and $Q_d = 5$ ml/h, the droplet length varies between around 500 and 520 μm, while at flow rates of the continuous and dispersed phases, respectively, of 8 and 4 ml/h, the length varies less widely, from about 520 to 530 μm. Furthermore, at $Q_c = 6.5$ ml/h and $Q_d = 4$ ml/h, changing the butanol viscosity has a negligible effect on the droplet length at all the viscosity values simulated. To verify this result, the viscosity was further increased. The droplet length decreased by a couple of microns at 0.007 kg/ms. In addition, the $D_h/75$ grid was used to confirm the effect. Similarly to $D_h/50$, the droplet size remained unchanged when modifying the dispersed phase viscosity within the tested range. A reason why the droplet length is not influenced due to the change in viscosity might be that the channel geometry limits the droplet size (Garstecki et al., 2006).

The water slug length changes in the following intervals (from higher to lower total flow rates): 517–577, 551–599, and 490–517 μm. The influence of the viscosity of the dispersed phase on the droplet formation is thus reduced with decreased flow rates.

Next, for the same cases as in Table 2, the viscosity of water was only varied to investigate the effect of the continuous phase viscosity. As Fig. 7a–c demonstrate, increasing the vis-

cosity of the continuous liquid results in decreased droplet size and water slug length. Such effects are attributed to larger shear stresses exerted on the dispersed phase thread by the more viscous continuous phase. As illustrated in Fig. 7d, a more viscous continuous phase contributes to the elongation of the dispersed phase thread in the main channel, thus leading to the formation of smaller droplets and shorter slugs. The experimental observations of Wu et al. (2017b) support the present results.

4.6. Effect of interfacial tension

Another important property that affects the droplet generation process is the interfacial tension. Similarly as in the previous section, the interfacial tension of water–butanol systems given in Table 2 was modified while keeping the other properties constant. As mentioned previously, the interfacial tension force counteracts the droplet formation, hindering the elongation of the dispersed phase thread. The effect is illustrated in Fig. 8a. The droplets thus detach less easily at the higher values of the interfacial tension. Therefore, as shown in Fig. 8b–d, the formation frequency decreases (i.e., the water slug length increases) and the droplet size increases with increasing interfacial tension.

The results indicate that the droplet and slug sizes can be adjusted by modifying the interfacial tension between the liquids. In experiments, the interfacial tension can be, for example, decreased by adding surfactants (Baret, 2012).

5. Summary and conclusions

CFD modeling and analysis of the droplet generation process in a cross-shaped square microchannel of 400 μm diameter were carried out for a range of flow conditions using the VOF method. Two immiscible liquid–liquid flow systems were

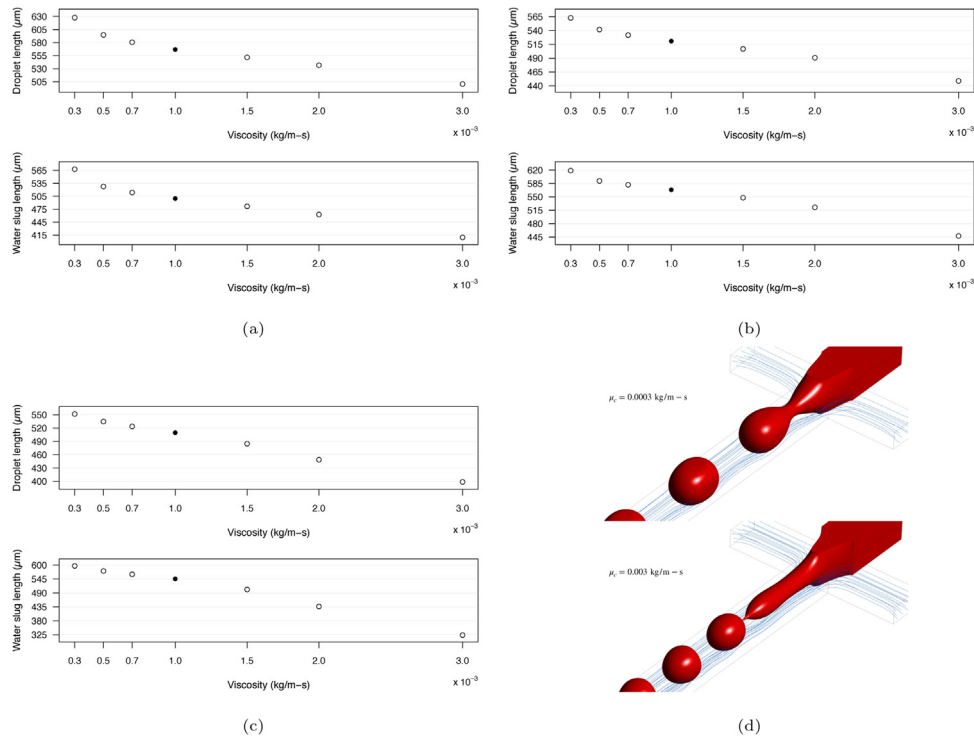


Fig. 7 – Effect of the continuous phase viscosity on the droplet and water slug lengths for water–butanol flow. (a) $Q_c = 6.5$ ml/h, $Q_d = 4$ ml/h; (b) $Q_c = 8$ ml/h, $Q_d = 4$ ml/h; (c) $Q_c = 10$ ml/h, $Q_d = 5$ ml/h; (d) less viscous (top) and more viscous (bottom) continuous phase at $Q_c = 10$ ml/h, $Q_d = 5$ ml/h. Filled circle denotes the original viscosity of water.

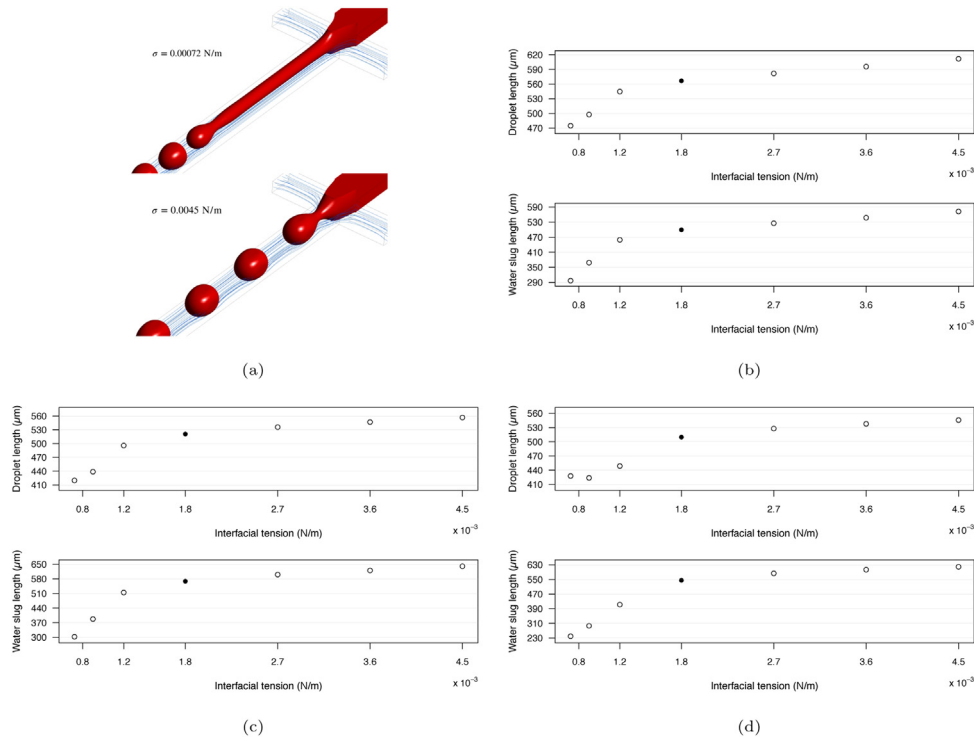


Fig. 8 – Effect of the interfacial tension on the droplet and water slug lengths for water–butanol flow. (a) lower (top) and higher (bottom) interfacial tension at $Q_c = 10$ ml/h, $Q_d = 5$ ml/h; (b) $Q_c = 6.5$ ml/h, $Q_d = 4$ ml/h; (c) $Q_c = 8$ ml/h, $Q_d = 4$ ml/h; (d) $Q_c = 10$ ml/h, $Q_d = 5$ ml/h. Filled circle denotes the original interfacial tension between water and butanol.

considered: water–butanol and water–toluene, with water as the continuous phase. The systems were visualized experimentally and simulated over a range of flow conditions by varying the flow rates of the phases ($1.9 \times 10^{-4} \leq Ca_c \leq 9.6 \times 10^{-3}$, $2.9 \times 10^{-5} \leq We_d \leq 1.3 \times 10^{-2}$). The effect of the viscosity of the dispersed and continuous phases and the interfacial tension between the phases on the droplet generation was analyzed

numerically for the water–butanol system. The slug flow dynamics obtained numerically were in agreement with the experimental findings.

The numerical setup was also employed to model the droplet generation in a T-shaped microchannel (Garstecki et al., 2006). The modeled droplet size and slug length were predicted accurately for a range of flow rates, while in some

cases the actual flow regime was not captured properly. The findings obtained from the T-junction simulations thus suggested that the use of a dynamic contact angle may be critical to model the slug flow regime correctly. Future work would then include experiments and simulations over a wider range of cases to carry out a more comprehensive investigation of the issue.

A set of measures was applied to increase the speed of the simulations. The mesh independence analysis showed that a relatively coarse grid can be used while preserving the overall accuracy of the calculations (grids with the element size of down to 1/100 of the hydraulic diameter were tested). The following steps were also taken to minimize the computational expenses:

- Reducing the original channel length and applying symmetry planes.
- Increasing the cell size in the inlet direction where surface tension forces are of no importance.
- Defining fully-developed velocity profiles at the inlets to further shorten the inlet channel lengths.
- Initial filling of the dispersed phase channel with the respective liquid phase.
- Setting a contact angle at the main channel boundaries to capture the liquid film without applying a too fine mesh.
- Employing a non-iterative time-advancement algorithm.
- Use of an adaptive time step control based on Courant number.

In summary, the proposed numerical setup can be utilized to model the process of droplet formation in microchannels over a wide range of conditions. The computed droplet and slug sizes can then be utilized to study such phenomena as heat transfer and mixing. Furthermore, it possesses good potential to offer a practical opportunity for development of chips for droplet generation by testing virtual prototypes. Owing to the capability of performing fast calculations, time savings in the research and design phases can thus be considerable.

Declaration of Competing Interest

The authors report no declarations of interest.

Acknowledgments

The authors wish to acknowledge CSC-IT Center for Science, Finland, for providing computational resources. Part of the work was carried out as RF was a visiting doctoral student at Lund University. RF acknowledges Prof. Heikki Haario for support and discussions.

Appendix A. Supplementary data

Supplementary data associated with this article can be found, in the online version, at <https://doi.org/10.1016/j.cherd.2020.11.010>.

References

- Abdollahi, A., Sharma, R.N., Vatani, A., 2017. Fluid flow and heat transfer of liquid–liquid two phase flow in microchannels: a review. *Int. Commun. Heat Mass Transfer* 84, 66–74.
- Asadolahi, A.N., Gupta, R., Fletcher, D.F., Haynes, B.S., 2011. CFD approaches for the simulation of hydrodynamics and heat transfer in Taylor flow. *Chem. Eng. Sci.* 66, 5575–5584.
- Baret, J.C., 2012. Surfactants in droplet-based microfluidics. *Lab Chip* 12, 422–433.
- Bordbar, A., Taassob, A., Zarnaghsh, A., Kamali, R., 2018. Slug flow in microchannels: numerical simulation and applications. *J. Ind. Eng. Chem.* 62, 26–39.
- Brackbill, J., Kothe, D.B., Zemach, C., 1992. A continuum method for modeling surface tension. *J. Comput. Phys.* 100, 335–354.
- Bretherton, F.P., 1961. The motion of long bubbles in tubes. *J. Fluid Mech.* 10, 166–188.
- Che, Z., Wong, T.N., Nguyen, N.T., Yang, C., 2015. Three dimensional features of convective heat transfer in droplet-based microchannel heat sinks. *Int. J. Heat Mass Transfer* 86, 455–464.
- Dang, M., Yue, J., Chen, G., 2015. Numerical simulation of Taylor bubble formation in a microchannel with a converging shape mixing junction. *Chem. Eng. J.* 262, 616–627.
- Fang, C., Hidrovo, C., Wang, F.m., Eaton, J., Goodson, K., 2008. 3-D numerical simulation of contact angle hysteresis for microscale two phase flow. *Int. J. Multiphase Flow* 34, 690–705.
- Fletcher, D.F., McClure, D.D., Kavanagh, J.M., Barton, G.W., 2017. CFD simulation of industrial bubble columns: numerical challenges and model validation successes. *Appl. Math. Modell.* 44, 25–42.
- Garstecki, P., Fuerstman, M.J., Stone, H.A., Whitesides, G.M., 2006. Formation of droplets and bubbles in a microfluidic T-junction-scaling and mechanism of break-up. *Lab Chip* 6, 437–446.
- Geng, Y., Ling, S., Huang, J., Xu, J., 2020. Multiphase microfluidics: Fundamentals, Fabrication, and Functions. *Small* 16, 1906357.
- Gupta, R., Fletcher, D.F., Haynes, B.S., 2009. On the CFD modelling of Taylor flow in microchannels. *Chem. Eng. Sci.* 64, 2941–2950.
- Gupta, R., Fletcher, D.F., Haynes, B.S., 2010. CFD modelling of flow and heat transfer in the Taylor flow regime. *Chem. Eng. Sci.* 65, 2094–2107.
- Gupta, R., Leung, S.S., Manica, R., Fletcher, D.F., Haynes, B.S., 2013. Hydrodynamics of liquid–liquid Taylor flow in microchannels. *Chem. Eng. Sci.* 92, 180–189.
- Hirt, C.W., Nichols, B.D., 1981. Volume of fluid (VOF) method for the dynamics of free boundaries. *J. Comput. Phys.* 39, 201–225.
- Hoang, D.A., van Steijn, V., Portela, L.M., Kreutzer, M.T., Kleijn, C.R., 2013. Benchmark numerical simulations of segmented two-phase flows in microchannels using the volume of fluid method. *Comput. Fluids* 86, 28–36.
- Huhtamäki, T., Tian, X., Korhonen, J.T., Ras, R.H., 2018. Surface-wetting characterization using contact-angle measurements. *Nat. Protoc.* 13, 1521.
- Jia, H., Zhang, P., 2016. Investigation of the Taylor bubble under the effect of dissolution in microchannel. *Chem. Eng. J.* 285, 252–263.
- Kandlikar, S., Garimella, S., Li, D., Colin, S., King, M.R., 2005. *Heat Transfer and Fluid Flow in Minichannels and Microchannels*. Elsevier.
- Kumari, S., Kumar, N., Gupta, R., 2019. Flow and heat transfer in slug flow in microchannels: effect of bubble volume. *Int. J. Heat Mass Transfer* 129, 812–826.
- Lan, W., Li, S., Luo, G., 2015. Numerical and experimental investigation of dripping and jetting flow in a coaxial micro-channel. *Chem. Eng. Sci.* 134, 76–85.
- Langewisch, D., Buongiorno, J., 2015. Prediction of film thickness, bubble velocity, and pressure drop for capillary slug flow using a CFD-generated database. *Int. J. Heat Fluid Flow* 54, 250–257.
- Madelahhi, M., Shamlou, A., 2017. Droplet-based flows in serpentine microchannels: chemical reactions and secondary flows. *Int. J. Multiphase Flow* 97, 186–196.
- Magnini, M., Thome, J., 2016. A CFD study of the parameters influencing heat transfer in microchannel slug flow boiling. *Int. J. Thermal Sci.* 110, 119–136.

- Mehdizadeh, A., Sherif, S., Lear, W., 2011. Numerical simulation of thermofluid characteristics of two-phase slug flow in microchannels. *Int. J. Heat Mass Transfer* 54, 3457–3465.
- Nguyen, N.T., Wereley, S.T., Shaegh, S.A.M., 2019. *Fundamentals and Applications of Microfluidics*, 3rd ed. Artech House.
- Qian, J.Y., Li, X.J., Wu, Z., Jin, Z.J., Zhang, J., Sundén, B., 2019. Slug formation analysis of liquid–liquid two-phase flow in T-junction microchannels. *J. Thermal Sci. Eng. Appl.* 11, 051017.
- Rajesh, V., Buwa, V.V., 2018. Volume-of-fluid simulations of gas–liquid–liquid flows in minichannels. *Chem. Eng. J.* 345, 688–705.
- Soh, G.Y., Yeoh, G.H., Timchenko, V., 2016. Numerical investigation on the velocity fields during droplet formation in a microfluidic T-junction. *Chem. Eng. Sci.* 139, 99–108.
- Song, H., Chen, D.L., Ismagilov, R.F., 2006. Reactions in droplets in microfluidic channels. *Angew. Chem. Int. Ed.* 45, 7336–7356.
- Taha, T., Cui, Z., 2006. CFD modelling of slug flow inside square capillaries. *Chem. Eng. Sci.* 61, 665–675.
- Talimi, V., Muzychka, Y., Kocabiyik, S., 2013. Slug flow heat transfer in square microchannels. *Int. J. Heat Mass Transfer* 62, 752–760.
- Wang, J., Wang, J., Feng, L., Lin, T., 2015. Fluid mixing in droplet-based microfluidics with a serpentine microchannel. *RSC Adv.* 5, 104138–104144.
- Wu, L., Liu, X., Zhao, Y., Chen, Y., 2017a. Role of local geometry on droplet formation in axisymmetric microfluidics. *Chem. Eng. Sci.* 163, 56–67.
- Wu, Z., Cao, Z., Sundén, B., 2017b. Liquid–liquid flow patterns and slug hydrodynamics in square microchannels of cross-shaped junctions. *Chem. Eng. Sci.* 174, 56–66.
- Yokoi, K., Vadillo, D., Hinch, J., Hutchings, I., 2009. Numerical studies of the influence of the dynamic contact angle on a droplet impacting on a dry surface. *Phys. Fluids* 21, 072102.
- Youngs, D.L., 1982. Time-dependent multi-material flow with large fluid distortion. *Numer. Methods Fluid Dyn.*, 273–285.
- Zhang, J., Fletcher, D.F., Li, W., 2016. Heat transfer and pressure drop characteristics of gas–liquid Taylor flow in mini ducts of square and rectangular cross-sections. *Int. J. Heat Mass Transfer* 103, 45–56.